Supplementary Information

Nitrogen doping boosted aqueous Zn-CO_2 batteries producing methane and electricity simultaneously

Rani Misbah,[1,#] Di Li,[1,#] Hameed Sidra,[1] Muhammad Ehtasham Ul Haq,[2] Tengda Lu,[1] Sheng Chen,[2] Qiang Li,[1] and Jingjing Duan[1,*]

[1]MIIT Key Laboratory of Thermal Control of Electronic Equipment, School of Energy and Power Engineering, Nanjing University of Science and Technology, Nanjing, 210094, China

[2]School of Chemistry and Chemical Engineering, Nanjing University of Science and Technology, Nanjing, 210094, China

E-mail: jingjing.duan@njust.edu.cn

1. Figure and Table Captions

Figure S1. The Cu-BTC material: (a) SEM image and (b) EDX mapping images of Cu, O and C elements.

Figure S2. XPS survey spectra of the (a) Cu-BTC and (b) N-Cu-BTC catalyst.

Figure S3. The O 1s XPS spectra of Cu-BTC and N-Cu-BTC.

Figure S4. Photographs of (a) the nickel-foam counter electrode, (b) the catalyst-coated working electrode and (c) schematic illustration of the three-chamber flow-type eCO_2RR cell assembly.

Figure S5. (a) CV and (b) LSV curves of eCO_2RR promoted by Cu-BTC and N-Cu-BTC.

Figure S6. (a) EF_{CH4} and (b) FE_{H2} of eCO_2RR catalyzed by Cu-BTC and N-Cu-BTC.

Figure S7. Tafel plots of eCO_2RR catalyzed by Cu-BTC and N-Cu-BTC.

Figure S8. Partial current density for CH_4 formation during eCO_2RR catalyzed by Cu-BTC and N-Cu-BTC.

Figure S9: The step diagram corrected by VASPSOL considering the solvation effect.

Figure S10. (a) The Zn anode and (b) N-Cu-BTC working electrode used in the three-chamber flow-type AZCB.

Figure S11. (a) OCP curves of the Cu-BTC constructed AZCB against CO_2 and Ar gases; (b) Discharge response along power density.

Figure S12. (a) Polarization charge and discharge curves and (b) Power density curves for AZCBs using Cu-BTC and N-Cu-BTC.

Figure S13. Comparison of power densities between this work and reported data with CH_4 as the eCO_2RR product.

Figure S14. The galvanostatic cyclability curve at a current density of 0.5 mA cm^{-2} for Cu-BTC.

Figure S15. Digital photograph for single bulb illuminated by three series of an N-Cu-BTC AZCBs.

Table S1. Comparison of FE_{CH4} of eCO_2RR using as prepared electrode.

Table S2. Comparison of practical discharge capacity and Zn utilization of the Zn–CO_2 battery with the theoretical Zn capacity at different discharge currents.

Table S3. Comparison of aqueous Zn-CO_2 battery performance with reported data.

2. Experimental Section

2.1 Chemicals

The reagents included: copper nitrate ($Cu(NO_3)_2{\cdot}3H_2O$, 98%, (Sigma-Aldrich)1,3,5-benzenetricarboxylic acid (H_3BTC, 99%, (Sigma-Aldrich), absolute ethanol (C_2H_5OH, 99) were purchased from SCR, Chemical (ptv) Ltd, urea ($CO(NH_2)_2$, 99%, (Sigma-Aldrich), nitrogen gas (N_2, 99.99%, Linde) . Nafion and de-ionized water, carbon dioxide (CO_2 99.999%) purity were used. All chemicals are analytical grade and used without any further purification.

2.2 Materials synthesis

2.2.1 Synthesis of Cu-BTC

Generally, Cu-BTC was synthesized via a solvothermal process. To begin, 2.0 g of copper nitrate trihydrate was dissolved in 50 mL of ethanol, while 1.0 g of 1,3,5-benzenetricarboxylic acid (H_3BTC) was dissolved in a mixture of 30 mL of ethanol and 20 mL of deionized (DI) water. Above solutions were stirred separately to ensure complete dissolution, and then mixed by stirring for 15 minutes to form a homogeneous precursor solution. This solution was transferred into a 100 mL Teflon-lined stainless-steel autoclave, sealed tightly, and heated at 80 °C for 72 hours for crystal growth. After which, the autoclave is allowed to cool naturally to room temperature. The blue crystalline product is obtained by vacuum filtration. To eliminate any residual unreacted precursors or impurities, the solid product is washed three times with ethanol and then dried in a vacuum oven at 80 °C for 12 hours.

2.2.2 Synthesis of N-Cu-BTC

N-doped Cu-BTC was synthesized *via* a post-incorporation strategy using urea as the nitrogen source. In detail, pristine Cu-BTC was dispersed in an ethanol-DI water mixture, followed by addition of urea to ensure uniform interactions with MOF, and the suspension was then subjected to solvothermal treatment at 80 °C for 12 hours. During this process, urea gradually decomposed to provide nitrogen species that were incorporated into the ligand environment and coordinated with unsaturated Cu sites, resulting in effective nitrogen doping while maintaining the structural integrity of the framework. After cooling, the product was collected, thoroughly washed with ethanol, and vacuum-dried at 80 °C for 12 hours to obtain N-Cu-BTC.

2.3 Physical characterizations

The crystal structure of the as-prepared materials was also examined by powder X-ray diffraction analysis (XRD, Bruker AXS) at a scanning rate of 5°/min in the range of 20° to 80°. Fournier transform infrared (FTIR) spectroscopy was performed using an FTIR, Nicolet 6700, spectrometer. The surface morphologies and microstructural analysis of the materials were determined using Scanning Electron Microscopy (SEM, Hitachi S-4800 II, Japan). Energy-dispersive X-ray Spectroscopy (EDX) was used in conjunction with scanning electron microscopy (SEM) to obtain elemental composition analysis. X-ray Photoelectron Spectroscopy (XPS) was performed using a PHI 500 ESCA spectrometer to investigate the surface chemical states.

2.4 Electrochemical measurements of eCO_2RR

Electrochemical testing of eCO_2RR was conducted in a three-chamber flow-type electrolyser using a CHI electrochemical workstation (CHI 760E). The working electrode was prepared by coating the catalyst ink onto carbon paper with an exposed area of 1×1 cm^2 and a catalyst loading of 10 mg cm^{-2}. A nickel-foam electrode and an Ag/AgCl/saturated KCl electrode were used as the counter and reference electrodes, respectively. The electrolyte was 1 M KOH, and CO_2 was continuously supplied at 80 mL min^{-1} to maintain saturation during eCO_2RR. The anodic and cathodic chambers were separated by an FAA-3-50 anion-exchange membrane (Fumasep), which provided ionic conduction while minimizing electrolyte crossover. Cyclic voltammetry (CV) was performed at a scan rate of 0.1 V/s in the potential range of 0.0 V to -3.0 V (vs. reversible hydrogen electrode, RHE). Linear sweep voltammetry (LSV) was conducted with a scan rate of 0.01 V/s from 0 V to -3.0 V vs RHE. Electrochemical impedance (EIS) measurement was conducted over a frequency range of 0.01Hz to 10^6 Hz at an applied potential of -2.25V. All potentials were calibrated relative to the RHE using the equation:

$$E_{RHE} = E_{Ag/AgCl} + 0.0591 \times pH + 0.197\ V$$

To further evaluate the reaction kinetics of the catalysts, Tafel plots were derived from the polarization data. The fitted Tafel slopes are 230 mV dec^{-1} for Cu-BTC and 160 mV dec^{-1} for N-Cu-BTC, indicating faster interfacial charge-transfer kinetics after nitrogen doping. In addition, the partial current density for CH_4 was calculated from the total current density and the corresponding FE_{CH4} values at different applied potentials. N-Cu-BTC exhibits a higher CH_4 partial current density than Cu-BTC over the investigated potential range, further confirming its superior catalytic activity and selectivity toward CH_4 formation.

Tafel plots were constructed by plotting potential (V vs RHE) against log10(j) and fitting the linear, kinetically controlled region (0.05-0.30 mA cm^{-2}) to the Tafel equation:

$$E = a + b \times \log10(j)$$

where b is the Tafel slope.

2.5 Analysis of eCO_2RR products

The gaseous products of eCO_2RR were quantified using gas chromatography (GC), equipped with a thermal conductivity detector (TCD) for measuring H_2 and a flame ionization detector (FID) for measuring aliphatic hydrocarbons, such as CH_4 and C_2H_4. Calibration was conducted using reference gas mixtures with an established concentration for the calibration of each product. The Faraday efficiency (FE), current density, and selective reduction of CO_2 to CH_4 were investigated by applying over-potentials in a potential range of -1.0 V to -2.75 V vs RHE. The following formula can calculate the FE of products:

$$FE(\%) = \left(\frac{n \times N_{product} \times F}{Q_{total}}\right) \times 100$$

- n is the number of electrons transferred during eCO_2RR
- F is the Faraday constant (96485 C mol^{-1})
- N is the number of moles of product
- Q total is the total charge passed

CH_4 was quantified by gas chromatography during eCO_2RR under continuous CO_2 supply, providing strong evidence for CO_2-involved methane formation. In addition, isotope-tracing with labeled CO_2 offers a rigorous route for direct carbon-source verification; under alkaline conditions, this can be expressed as $^{13}CO_2 + 6H_2O + 8e^- \rightarrow {}^{13}CH_4 + 8OH^-$.

2.5.1 Discussion of reaction kinetics and selectivity at negative potentials

Although the optimal eCO_2RR performance was obtained at a relatively negative potential, the reaction was conducted in strongly alkaline 1 M KOH within a three-chamber flow-type electrolyser under continuous CO_2 supply. Under these conditions, the reduced proton concentration helps suppress HER, while the flow-type configuration improves CO_2 transport to the cathode. In addition, the carbon-paper substrate provides a relatively hydrophobic gas-diffusion interface, which helps maintain CO_2 access and limit water access to the catalytic sites, suppressing HER. More importantly, N-Cu-BTC exhibits faster interfacial kinetics than Cu-BTC, as evidenced by its lower charge-transfer resistance, higher Cdl, and smaller Tafel slope. In parallel, DFT calculations show that nitrogen incorporation lowers the free-energy barrier of the potential-determining $^*CO \rightarrow {}^*CHO$ step and enhances charge transfer between Cu sites and carbonaceous intermediates. These combined effects explain why CH_4 formation remains favored over HER even at relatively negative potentials.

2.5.2 Ar control experiment for CH_4 verification

To further examine the carbon origin of methane product, a control experiment was performed under identical eCO_2RR conditions using Ar gas instead of CO_2 as the feeding gas. GC-FID analysis shows a clear CH_4 peak under CO_2 flow, whereas no detectable CH_4 peak is observed under Ar flow. Because CH_4 is detected only in the presence of CO_2 and disappear completely under Ar, this comparison strongly supports that methane formation originates from CO_2 reduction rather than from background contamination or other carbon sources in the system.

2.6 Assembly of aqueous Zn-CO_2 Batteries

The Zn-CO_2 battery measurements were also carried out in a three-chamber flow-type cell under continuous CO_2 and electrolyte flow, with two electrodes. For the cathode, the catalyst ink was spray-coated onto carbon paper with an exposed area of 1 × 1 cm^2, corresponding to a catalyst loading of 10 mg cm^{-2}. A polished Zn plate was used as the anode. The catholyte was 1 M KOH, and the anolyte was 6 M KOH + 0.2 M $Zn(CH_3COO)_2$, which are separated by an FAA-3-50 anion-exchange membrane (Fumasep) acting as the ion-conducting separator enabling anion transport between the two compartments while minimizing electrolyte crossover. During operation, electrons were transferred through the external circuit, whereas charge balance across the battery was maintained by ion migration through the membrane. CO₂ was continuously introduced to the cathode side during battery operation to maintain catholyte saturation. The three-chamber flow-type design, together with flowing anolyte, catholyte, and gas, improve CO₂ utilization and reduces product crossover. Various performance parameters were evaluated for the battery, including the determination of the open-circuit potential (OCP) for stable performance and linear sweep voltammetry (LSV) for assessing discharging and charging capabilities at a scan rate of 5 mV/s.

2.7 Parameter calculation for aqueous Zn-CO_2 batteries

Theoretical energy efficiency can be calculated using the following equation:

$$EE=\frac{\Delta G_{output}}{\Delta G_{input}}=\frac{nE_{discharge}F+\Delta G_{CO_2\,splitting}}{nE_{charge}F}$$

$$\Delta G_{CO_2 spliting}=257.38\mathrm{kJmol^{-1}}$$

During the discharging process of AZCBs, the competitive hydrogen evolution reaction (HER) produces H₂, which affects the battery performance. The energy efficiency (EE) of AZCBs can be calculated as follows:

$$EE=\frac{\Delta G_{output}}{\Delta G_{input}}=\frac{nE_{discharge}F+FE_{CH_4}\times\Delta G_{CO_2 spliting}+FE_{HER}\times\Delta G_{H_2O spliting}}{nE_{charge}F}$$

$$\Delta G_{H_2Osplitting}=257.38\mathrm{KJmol^{-1}}$$

To calculate the theoretical potential (V) for AZCBs, the anodic and cathodic reactions are shown as follows.

For the cathodic discharging of AZCBs, the following reaction happen:

At the cathode: (1 M KOH), pH =14

$$CO_2+6H_2O+8e^-\rightarrow CH_4+8OH^-$$

$$E_c=E^{\theta}_{CO_2/CH_4}-\frac{RT}{nF}\ln\left[\frac{1}{\alpha^2_{H^+}}\right]=-0.65\mathrm{V}-\frac{8.314\times298.15}{8\times96485}\ln\frac{1}{\left(10^{-14}\right)^2\mathrm{V}}=\text{-0.857V}$$

Where $E^{\theta}_{CO_2/CH_4}=-0.65\mathrm{V}$ vs. SHE

At the anode: (6 M KOH + 0.2 M Zn ($CH_3COO)_2$)

For the anodic discharging of AZCBs, the following reaction happen.

$$Zn^{2+}+4OH^-\rightarrow Zn\left(OH\right)_4^{2-}+2e^-$$

$$Zn\left(OH\right)_4^{2-} \rightarrow ZnO + 2OH^- + H_2O$$

$$E_a = E^{\theta}_{ZnO(OH)_4^{2-}} - \frac{RT}{nF}\ln\left[\frac{\alpha_{Zn}}{\alpha_{Zn(OH)_4^{2-}}}\right] = -1.255\text{V} - \frac{8.314\times 298.15}{8\times 96485}\ln\left[\frac{1}{0.2}\right]\text{V} = -1.260\text{V}$$

$$E^{\theta}_{ZnO(OH)_4^{2-}} = -1.255\text{V vs SHE}$$

Therefore, the overall battery reaction during discharging is as follows:

$$4Zn + CO_2 + 2H_2O \rightarrow 4ZnO + CH_4$$

The theoretical potential of AZCBs should be calculated using the below equation:

$$E_{theo} = E_c - E_a = -0.857\text{V} - (-1.260\text{V}) = 0.403\text{V}$$

Whereas R is 8.314 J K^{-1} mol^{-1} (molar gas constant), T = 298.15 K, n = 8 (total number of electrons transferred per mole of product), F = 96485 C mol^{-1} (Faraday Constant), and α is the corresponding activity. The theoretical energy density can be calculated by multiplying the specific capacity by the theoretical potential of the system.

$$ED_{Zn-CO_2} = C_{Zn} \times E_{theo} = 825\text{mAh}^{-1} \times 0.418\text{V} = 332.4\text{Whkg}^{-1}$$

C_{Zn} is the theoretical energy density of AZCBs using Zn anodes.

Additionally, HER also occurs during battery discharging, competing with the CO_2-to-CH_4 electro conversion process.

$$2H^+ + 2e^- \rightarrow H_2$$

$$E_c = E^{\theta}_{H^+/H_2} - \frac{RT}{nF}\ln\left[\frac{\alpha_{H_2}}{\alpha^2_{H^+}}\right] = -0.83\text{V} - \frac{8.314\times 298.15}{2\times 96485}\ln\left[\frac{1}{(10^{-14})^2}\right]\text{V} = \text{-}1.65\text{V}$$

$$E^{\theta}_{H^+/H_2} = \text{-}0.83\text{V vs. SHE}$$

The overall reaction of the discharging process along Zn oxidation and HER:

$$Zn + 2H^+ + 2OH^- \rightarrow ZnO + H_2 + H_2O$$

$$E^{'}_{theo} = E^{'}_c - E_a = -1.65\text{V} - (-1.260\text{V}) = \text{-}0.39\text{V}$$

During charging, water oxidation reaction happens at the cathode as follows.

$$4OH^- \rightarrow O_2 + 2H_2O + 4e^-$$

$$E^{''}_c = E^{\theta}_{H_2O/O_2} - \frac{RT}{nF}\ln\left[\frac{\alpha_{H_2O}}{\alpha_{O_2}^{1/2}\alpha^2_{H^+}}\right] = 1.229\text{V} - \frac{8.314\times 298.15}{4\times 96485}\ln\left[\frac{1}{1\times(10^{-14})^2}\right]V = 0.814\text{V}$$

Where,

$E^{\theta}_{H_2O/O_2}$ = 1.229V vs. SHE

While, the following reactions happen at the anode during charging.

$$Zn^{2+} + 4OH^{-} \rightarrow Zn\left(OH\right)_4^{2-} + 2e^{-}$$

$$Zn(OH)_4^{2-} + 2e^{-} \rightarrow Zn + 4OH^{-}$$

So, the overall reaction during charging is as follows:

$$2Zn(OH)_4^{2-} \rightarrow 2Zn + 2H_2O + 4OH^{-}$$

$$E^{''}_{theo} = E^{''}_{c} - E_{a} = 0.814\text{V} - (-1.26\text{ V}) = 2.077\text{V}$$

During discharge, the N-Cu-BTC-coated cathode catalyzes CO_2 reduction into CH_4 ($CO_2 + 8e + 6H_2O \rightarrow CH_4 + 8OH^{-}$), while the Zn electrode is oxidized ($Zn - 2e \rightarrow Zn^{2+}$) in the alkaline Zn-containing anolyte. While during charging, the reverse process occurs, in which zinc-containing species are reduced and re-deposited on the Zn electrode ($Zn^{2+} + 2e \rightarrow Zn$), while the counter reaction in the opposite alkaline compartment is water oxidation ($2H_2O - 4e \rightarrow O_2 + 4H^{+}$). The three-compartment cell configuration with an anion-exchange membrane minimizes crossover between the two electrode chambers. Moreover, charge and discharge are performed sequentially, so gaseous products generated during discharge are collected separately from the cathode outlet and were not directly mixed with those from the charging step.

2.7.1 Practical discharge capacity and Zn utilization

The practical discharge capacity of the Zn-CO_2 battery was calculated from the galvanostatic discharge current and discharge time according to Qpractical=I×t, where I is the discharge current and t is the discharge time. Using a Zn mass of 0.571 g and the theoretical specific capacity of Zn (820 mAh g^{-1}), the theoretical capacity was calculated to be 468 mAh. Based on a fixed discharge time of 0.083 h (5 min), the practical capacities at 1–5 mA were 0.083, 0.166, 0.250, 0.333, and 0.416 mAh, respectively, corresponding to specific capacities of 0.145, 0.291, 0.437, 0.583, and 0.729 mAh g^{-1} and Zn utilizations of 0.017, 0.035, 0.053, 0.071, and 0.088%, respectively. These low utilization values reflect the short discharge intervals used for proof-of-concept battery evaluation rather than full Zn consumption.

2.7.2 Discussion of the FE_{CH4} difference between the three-electrode eCO_2RR system and the AZCB device

The lower FE_{CH4} observed in the AZCB device compared with the maximum value achieved in the three-electrode eCO_2RR system mainly arises from the fundamentally different operating conditions of these two configurations. In the three-electrode flow electrolyser, the cathode potential can be independently controlled and optimized, allowing electron transfer to be directed more selectively toward the CO_2-to-CH_4 pathway. By contrast, in the full two-electrode AZCB, the cathodic eCO_2RR is coupled with Zn oxidation, governed by the overall battery discharge process including current load, internal resistance, ion transport, and gas-supply conditions. Consequently, the cathodic electron flow is less selectively utilized for CH_4 formation and is more strongly influenced by polarization losses and competing HER during practical battery operation. Moreover, the lower CO_2 flow rate in the AZCB further limits local CO_2 availability at the cathode interface, leading to a lower FE_{CH4} than that observed in the optimized half-cell measurement.

3. Computational methods

When studying the N-Cu-BTC catalyst, computational techniques were employed in parallel with experimental data to provide theoretical insights into the structure and electron configuration of the catalyst. The methods incorporated density functional theory estimates and structural optimization to simulate the supporting role of the catalyst in heterogeneous catalytic and electrochemical processes.

In the first stage, the structure of N-Cu-BTC was simulated using data extracted from the diffraction patterns of the unit cell and SEM images. These XRD patterns were used for the identification of the crystal structure and lattice parameters of both the parent Cu-BTC and the nitrogen-doped N-Cu-BTC framework. Therefore, the crystal face of the structure was cut and enlarged to simulate the material's behavior in both the bulk and at the surface. Based on the XPS analysis, the presence of nitrogen species in N-Cu-BTC was considered. Further, it introduced the nitrogen functional groups to the theoretical model by modifying the ligand framework.

The computational calculations were performed using the MedeA-VASP package, applying density functional theory (DFT) with a plane-wave basis set. The electron-ion interactions were treated within the projector augmented wave (PAW) method, while the electron-electron exchange-correlation interactions were described using the PBE functional. This functional, belonging to the category of the generalized gradient approximation (GGA), was designed to achieve a reasonable computational time and acceptable accuracy in describing the structural and electronic characteristics.

For structure optimization, the RMM-DIIS technique was employed to maintain high computational speed while minimizing errors. The cutoff energy for the plane-wave method was 400 eV, and the integration thresholds for electronic self-consistent iterations and ion optimization were 10^{-4} eV and 10^{-5} eV, respectively. Since the calculations of energy can be sensitive to the smearing width of partially occupied electronic states, a Gaussian smearing width of 0.05 eV was maintained in this work.

The Brillouin zone was sampled with a 1x1x1 Monkhorst-Pack grid, which was enough to seek the unit cell size of N-Cu-BTC. To incorporate information on strong electron correlation effects in the d-orbitals of the Cu atoms, Hubbard-U corrections (DFT+U) were employed to enhance the reliability of the model in transition metal-based systems.

Electron density maps and adsorption energy calculations were performed to study the adsorption of CO_2 on the N-Cu-BTC catalyst surface. The nitrogen doping sites were also examined to determine the new electron density and any potential for a new active site. Further, the atomic structure of the films proposed by the model was compared with real XRD patterns and electronic properties.

These computational methods enabled the revelation of structural characteristics, electronic properties, and catalytic activity of N-Cu-BTC, facilitating a better understanding of the performance benefits of N-Cu-BTC compared to Cu-BTC.

To better reflect the real electrocatalytic environment and clarify the limitations of the present DFT model, the following considerations were included in the revised analysis. In the present work, the DFT model was constructed using a simplified Cu-BTC unit-cell framework with idealized nitrogen incorporation in order to capture the dominant electronic-structure and reaction-energy trends at a computationally practical level. To better approximate the real aqueous electrocatalytic environment, the solvent effect was further considered using the VASPSOL implicit solvent model with a dielectric constant of 78.5. After introducing the solvent correction, the absolute energetics of the adsorbed intermediates were modified to some extent, but the overall mechanistic trend remained unchanged, namely that nitrogen incorporation lowers the free-energy barrier of the key *CO → *CHO step. The DFT results are interpreted as relative mechanistic trends rather than a complete quantitative description of the operating electrochemical interface.

4. Supporting Figures

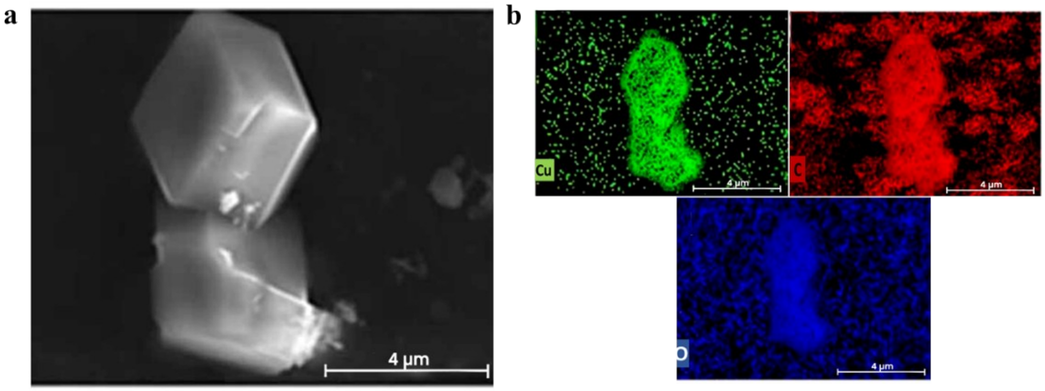

Figure S1. The Cu-BTC material: (a) SEM image and (b) EDX mapping images of Cu, O and C elements.

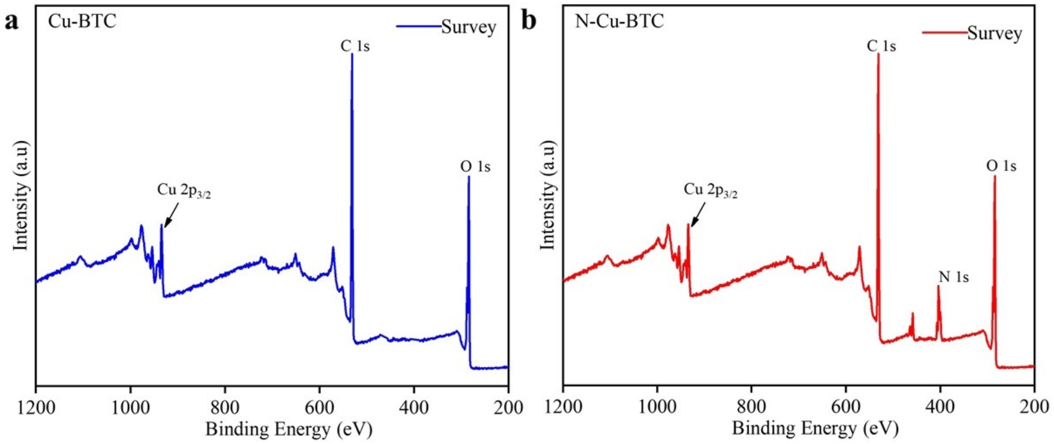

Figure S2. XPS survey spectra of the (a) Cu-BTC and (b) N-Cu-BTC catalyst.

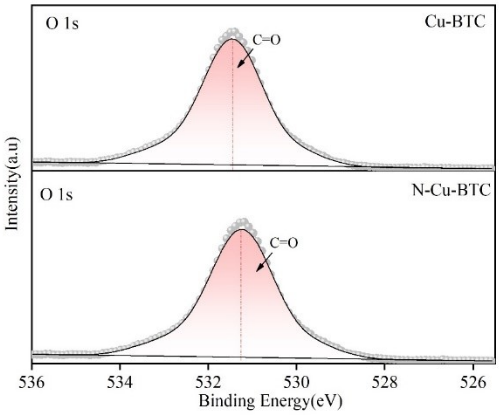

Figure S3. O 1s spectrum of Cu-BTC and N-Cu-BTC.

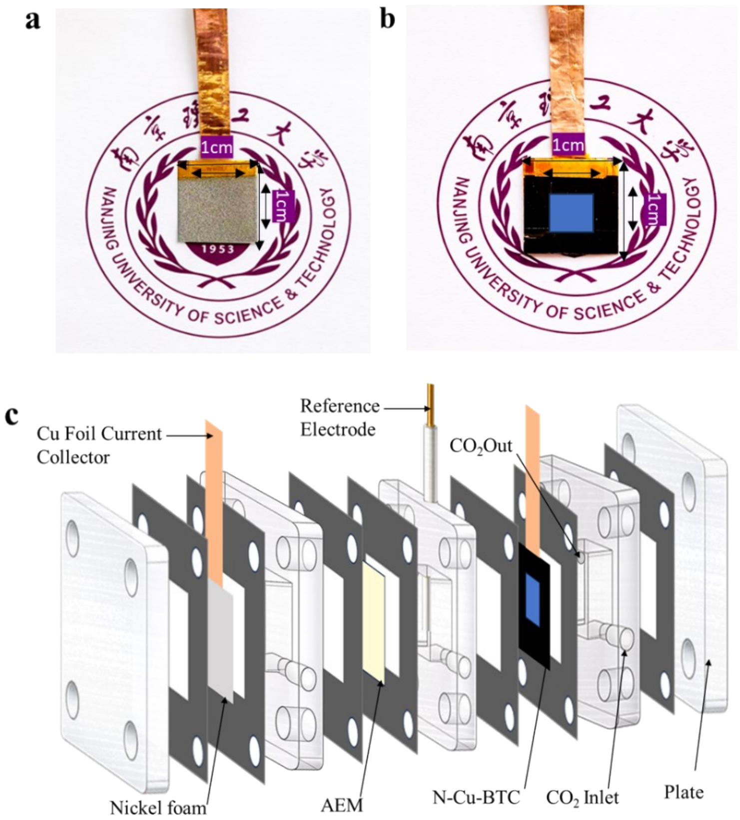

Figure S4. Photographs of (a) the nickel-foam counter electrode, (b) the catalyst-coated working electrode and (c) schematic illustration of the three-chamber flow-type eCO₂RR cell assembly. For battery testing, we remove the reference electrode and replace the nickel foam with Zn plates.

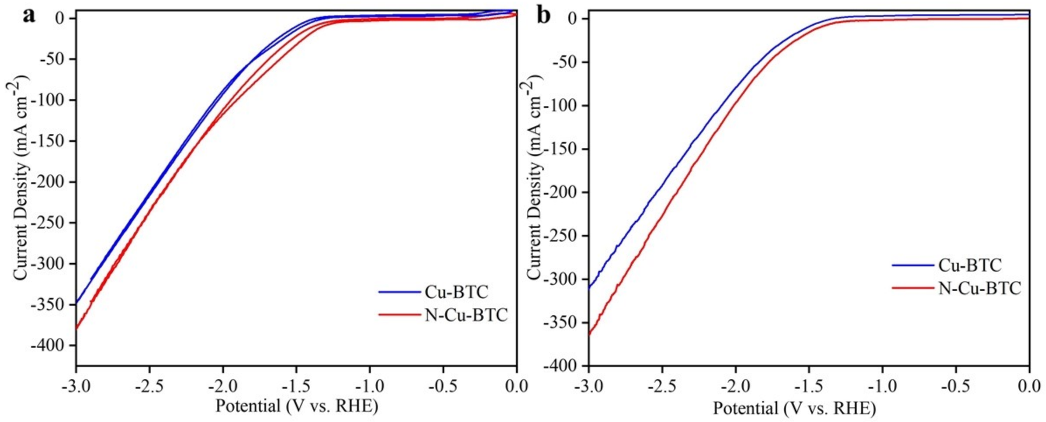

Figure S5. (a) CV and (b) LSV curves of eCO$_2$RR promoted by Cu-BTC and N-Cu-BTC.

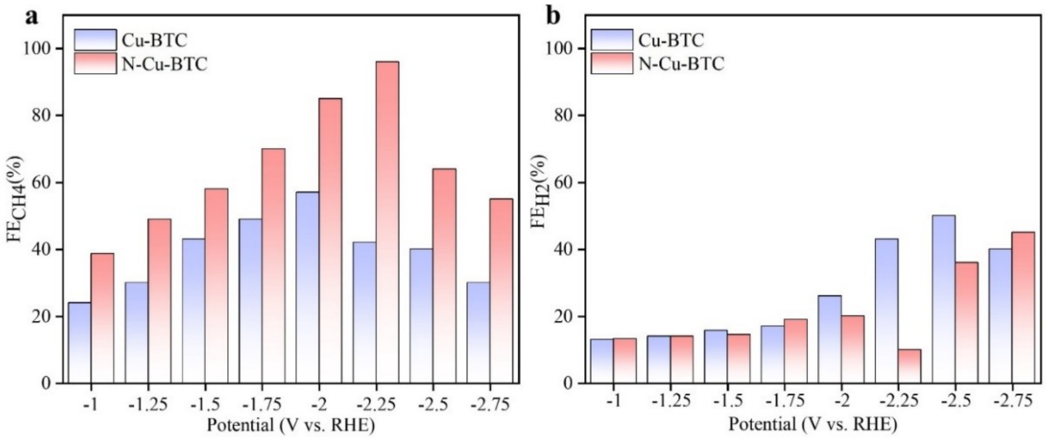

Figure S6. (a) EF_{CH4} and (b) FE_{H2} of eCO_2RR catalyzed by Cu-BTC and N-Cu-BTC.

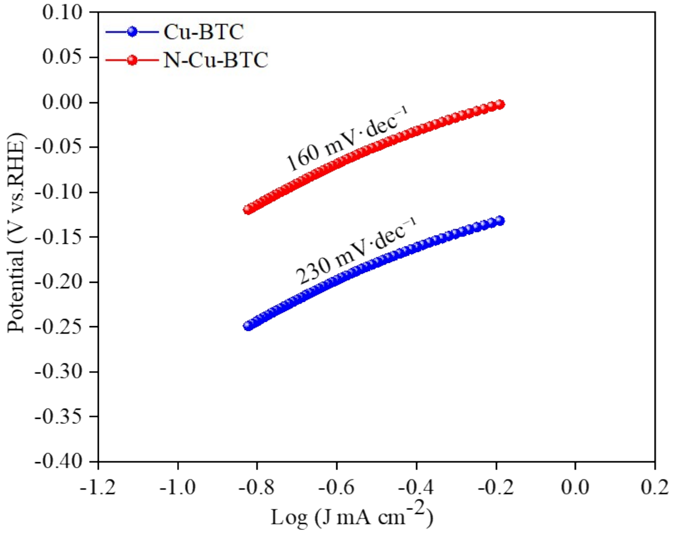

Figure S7. Tafel plots of eCO_2RR catalyzed by Cu-BTC and N-Cu-BTC.

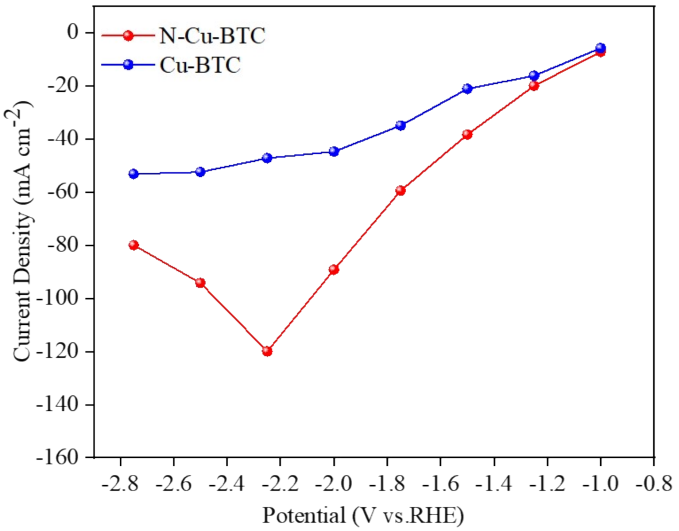

Figure S8. Partial current density for CH_4 formation during eCO_2RR catalyzed by Cu-BTC and N-Cu-BTC.

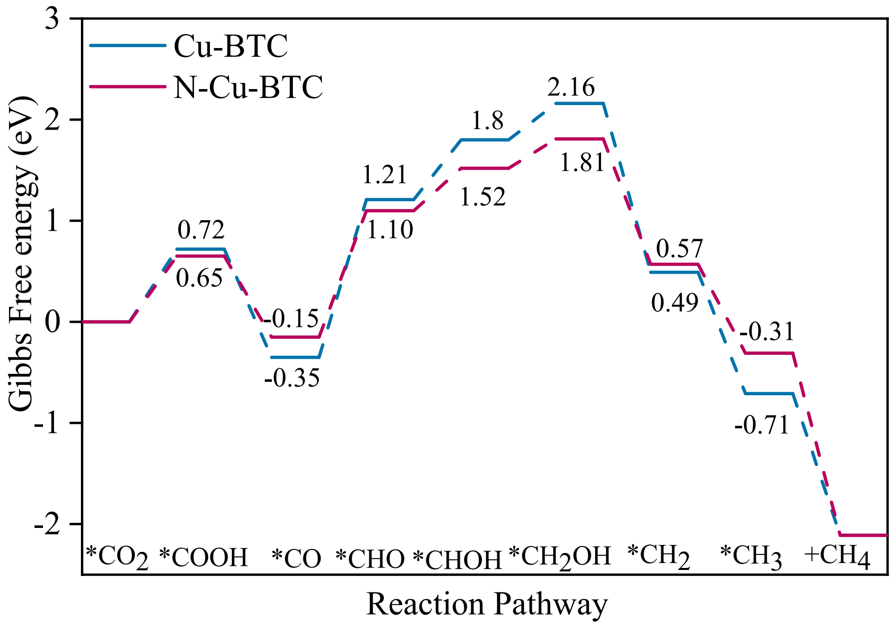

Figure S9: The reaction diagram corrected by VASPSOL considering the solvation effect.

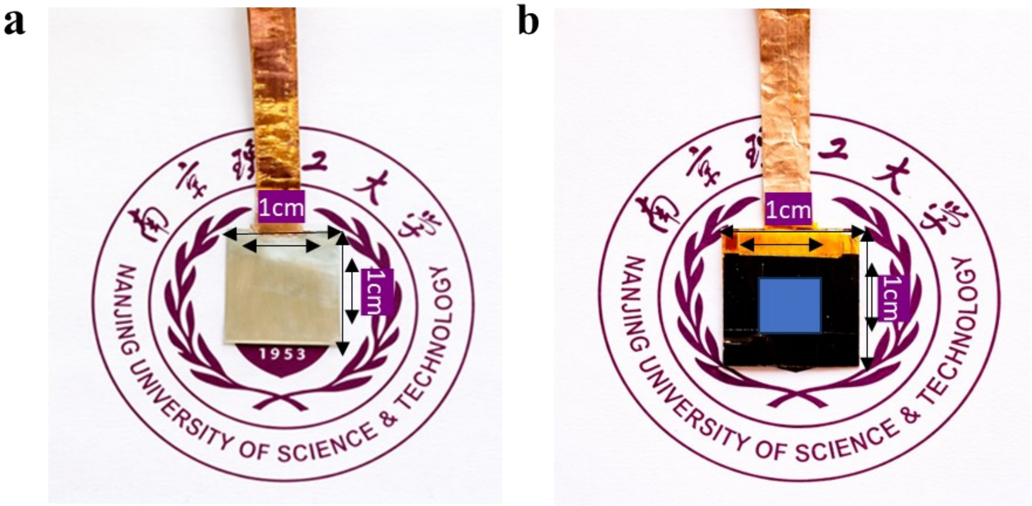

Figure S10. (a) The Zn anode and (b) N-Cu-BTC working electrode used in the three-chamber flow-type AZCB.

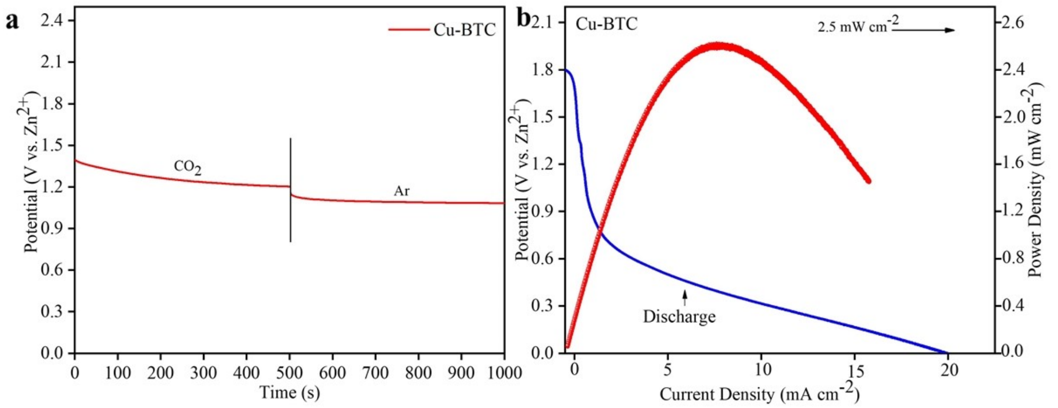

Figure S11. (a) OCP curves of the Cu-BTC constructed AZCB against CO_2 and Ar gases; (b) Discharge response along power density.

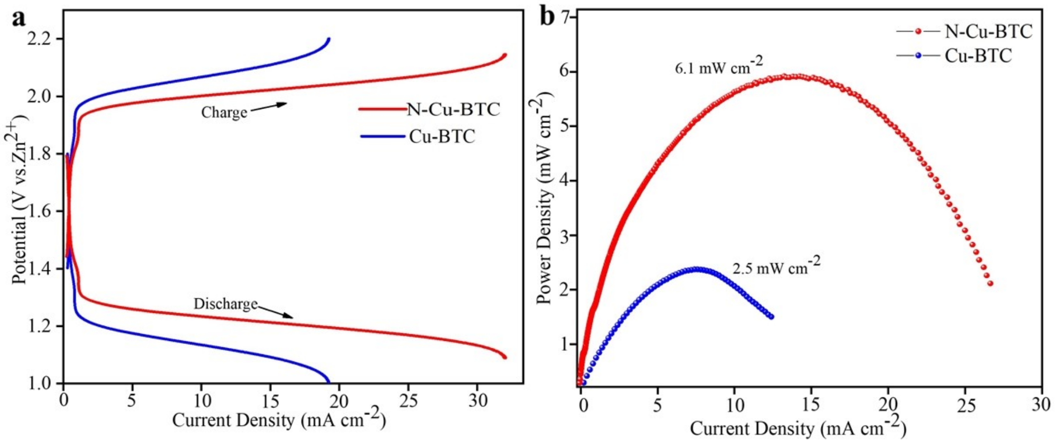

Figure S12. (a) Polarization charge and discharge curves and (b) Power density curves for AZCBs using Cu-BTC and N-Cu-BTC.

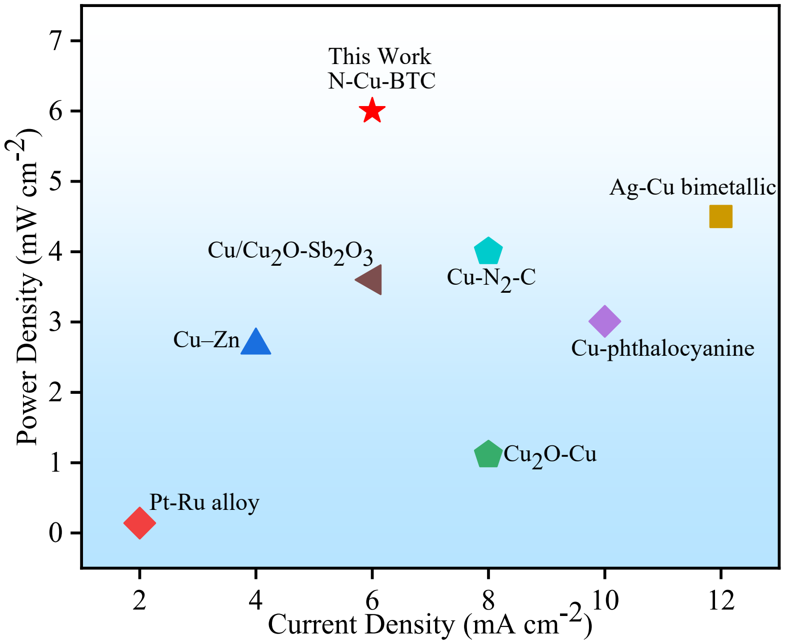

Figure S13. Comparison of power densities between this work and reported data with CH_4 as the eCO_2RR product.

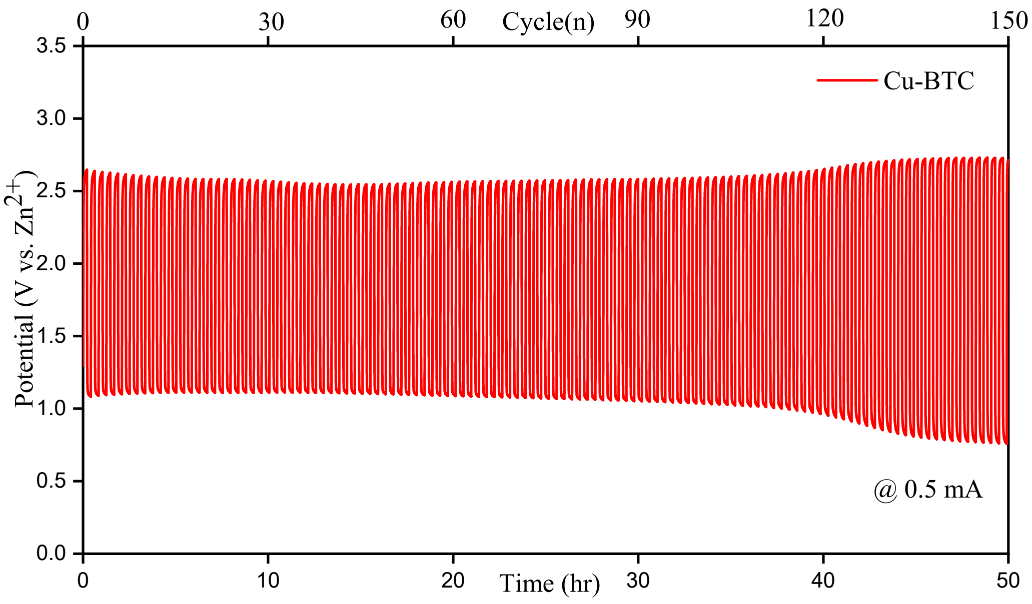

Figure S14. The galvanostatic cyclability curve at a current density of 0.5 mA cm^{-2} for Cu-BTC.

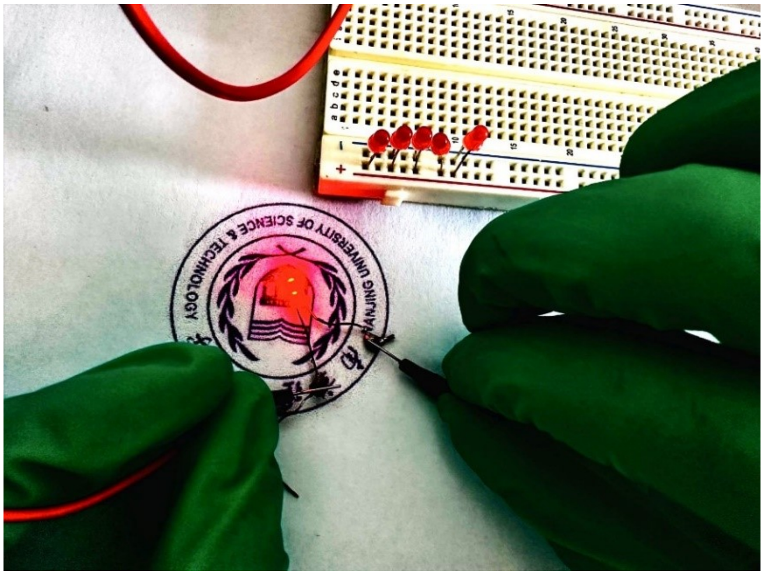

Figure S15. Digital photograph for single bulb illuminated by three series of an N-Cu-BTC AZCBs.

Table S1. Comparison of FE_{CH4} of eCO_2RR using as-prepared electrodes

Potential (V vs RHE)	Cu-BTC (CH_4) FE%	N-Cu-BTC(CH_4) FE%
-1.0	39	38.7
-1.25	45	49
-1.50	47	58
-1.75	50	70
-2.0	56	85
-2.25	45	96
-2.50	42	64
2.75	39	50

Table S2. Comparison of practical discharge capacity and Zn utilization of the Zn–CO_2 battery with the theoretical Zn capacity at different discharge currents

Current (mA)	Time (h)	Practical Capacity (mAh)	Specific Capacity (mAh g^{-1})	Zn Utilization (%)
0.5	*0.083*	*0.042*	*0.073*	*0.009*
1	*0.083*	*0.083*	*0.145*	*0.017*
2	*0.083*	*0.166*	*0.291*	*0.035*
3	*0.083*	*0.250*	*0.437*	*0.053*
4	*0.083*	*0.333*	*0.583*	*0.071*
5	*0.083*	*0.416*	*0.729*	*0.088*

340 **Table S3:** Comparison of aqueous Zn-CO_2 battery performance with reported data

Catalyst	**Electrolyte**	**Product**	**OCP**	**Discharge voltage (V)**	**Power density (mW cm^{-2})**	**Energy density (Wh kg^{-1})**	**Ref**
N-Cu-BTC	**Anolyte:** 1 M KOH + 0.2 M Zn(ac)$_2$ **Catholyte:** 1 M KOH	**CH_4**	**1.55**	**0.55**	**6.1 (15 mA cm^{-2})**	**332.4 Wh kg^{-1}**	**This work**
Fe_1NC/S-	**Anolyte:** 0.8 M KOH + 0.02 M Zn(ac)$_2$ **Catholyte:** 0.8 M $KHCO_3$	CO	0.72	0.21	0.52 (2.5 mA cm^{-2})	—	1
P-Ag/CP	**Anolyte:** 6 M KOH + 0.2 M Zn(ac)$_2$**Catholyte:** 0.8 M $KHCO_3$	CO	0.9	0.18	0.37 (2.1 mA cm^{-2})	—	2
Ni@NC	**Anolyte:** 6 M KOH + 0.2 M Zn(ac)$_2$ **Catholyte:** 1 M	CH_4	—	0.20	1.64 (8 mA cm^{-2})	—	3

	$KHCO_3$						
HPC–Co/CoPc	**Anolyte:** 6 M KOH + 0.2 M $Zn(ac)_2$ **Catholyte:** 1 M $KHCO_3$	CO	—	0.50	2.67 (10 mA cm^{-2})	533	4
VO-rich SnO_2 NS	**Anolyte:** 1 M KOH **Catholyte:** 0.1 M $KHCO_3$	Formate	—	1.00	3.67 (17 mA cm^{-2})	550	5
Cu_3P/C	**Anolyte:** 4 M NaOH **Catholyte:** 0.1 M $KHCO_3$	CO	1.4	0.25	2.6 (10 mA cm^{-2})	—	6
CuO/Cu-BTC	**Anolyte:** 1 M KOH **Catholyte:** 1 M KOH	C_2H_4 + CH_4	—	—	3.4	—	7
N-Cu-MOF NS	**Anolyte:** 0.5 M $KHCO_3$ **Catholyte:** 0.5 M $KHCO_3$	CH_4	—	—	2.9	—	8

Cu-BTC/Ag Hybrid	**Anolyte:** 6 M KOH + 0.2 M Zn(ac)$_2$ **Catholyte:** 0.8 M $KHCO_3$	CO + CH_4	—	—	2.1	—	9
Cu-BTC-derived Cu@C	**Anolyte:** 1 M KOH **Catholyte:** 1 M KOH	CH_4 + C_2H_4	—	—	4.8	—	10
Pd/SnO_2@C	**Anolyte:** 6 M KOH + 0.02 M Zn(ac)$_2$ **Catholyte:** 1 M $KHCO_3$	Formate	1.4	1.38	4.29 (8 mA cm^{-2})	827.3	11

References

1. S. Gao, T. Wei, J. Sun, Q. Liu, D. Ma, W. Liu, S. Zhang, J. Luo and X. Liu, Small Struct., 2022, 3, 2200086.
2. J. Xie, Q. Liu, Y. Huang, M. Wu and Y. Wang, J. Mater. Chem. A, 2018, 6, 13952–13958.
3. Y. Liu, J. Chen, W. Li, Y. Zhang, X. Fu, E. Li, S. Jin, L.-M. Yang, Z. Tian, M. Antonietti and T. Liu, Ind. Chem. Mater., 2024, 2, 514–532.
4. K. A. Adegoke and N. W. Maxakato, J. CO2 Util., 2023, 69, 102412.
5. X. Tan, S. Jia, X. Song, X. Ma, J. Feng, L. Zhang, L. Wu, J. Du, A. Chen, Q. Zhu, X. Sun and B. Han, Chem. Sci., DOI:10.1039/D3SC02790B.
6. M. Peng, S. Ci, P. Shao, P. Cai and Z. Wen, J. Nanosci. Nanotechnol., 2019, 19, 3232–3236.

7. Q. Wang, H. Wei, P. Liu, Z. Su and X.-Q. Gong, Nano Res. Energy, 2024, 3, e9120112.
8. Z. Yan, P. Gao, Z. Li, Y. Zhang, C. Hu, D. Cao and D. Cheng, Small, 2025, 21, 2500950.
9. S. Thoka, Z. Tong, A. Jena, T.-F. Hung, C.-C. Wu, W.-S. Chang, F.-M. Wang, X.-C. Wang, L.-C. Yin, H. Chang, S.-F. Hu and R.-S. Liu, J. Mater. Chem. A, 2020, 8, 23974–23982.
10. H. Wang, T. Wang, G. Dong, L. Zhang, F. Pan and Y. Zhu, Inorganics, 2025, 13, 130.
11. W. Guo, Y. Wang, Q. Yi, E. Devid, X. Li, P. Lei, W. Shan, K. Qi, L. Shi and L. Gao, Front. Energy Res., 2023, 11, 1194674.
12. Q. Cui, G. Qin, W. Wang et al., J. Mater. Chem. A, 2019, 7, 14510–14518.
13. T. Mueller and G. Ceder, J. Phys. Chem. B, 2005, 109, 17974–17983.
14. Z. Xing, L. Hu, D. S. Ripatti, X. Hu and X. Feng, Nat. Commun., 2021, 12, 136.
15. K. Yang, M. Li, T. Gao, G. Xu, D. Li, Y. Zheng, Q. Li and J. Duan, Nat. Commun., 2024, 15, 7060.